The origin of ferromagnetism in ^{57}Fe ion-implanted semiconducting 6H-polytype silicon carbide

2006 J. Phys.: Condens. Matter 18 9881

(http://iopscience.iop.org/0953-8984/18/43/010)

INSTITUTE OF PHYSICS PUBLISHING JOURNAL OF PHYSICS: CONDENSED MATTER

J. Phys.: Condens. Matter **18** (2006) 9881–9900 doi:10.1088/0953-8984/18/43/010

The origin of ferromagnetism in ^{57}Fe ion-implanted semiconducting 6H-polytype silicon carbide

F Stromberg[1], W Keune[1], X Chen[1], S Bedanta[1], H Reuther[2] and A Mücklich[2]

[1] Fachbereich Physik, Universität Duisburg-Essen, Lotharstrasse 65, D-47048 Duisburg, Germany
[2] Institut für Ionenstrahlphysik, Forschungszentrum Rossendorf, Bautzner Landstrasse 128, D-01328 Dresden, Germany

Received 1 August 2006, in final form 22 September 2006
Published 13 October 2006
Online at stacks.iop.org/JPhysCM/18/9881

Abstract

Semiconducting (mostly p-doped) single crystals of the 6H-polytype of α-SiC(0001) were implanted with ^{57}Fe ions with a nominal dose of 1.0×10^{16}, 2.0×10^{16}, 3.0×10^{16} or 2.0×10^{17} cm^{-2} (high-dose sample p-hd) at 100 or 200 keV ion energy in order to produce diluted magnetic semiconductors (DMSs). After implantation all samples (except p-hd) were subject to rapid thermal annealing at 1000 °C for 2 min. The structure was investigated by x-ray diffraction, high-resolution cross-sectional transmission electron microscopy and sputter-Auger depth profiling. The magnetic properties were obtained from superconducting quantum interference device (SQUID) magnetometry and ^{57}Fe conversion electron Mössbauer spectroscopy (CEMS) at room temperature (RT) and 4.2 K. Our combined results obtained by several techniques prove unambiguously that ferromagnetism in ^{57}Fe-implanted SiC for Fe concentrations above 3% originates mostly from epitaxial superparamagnetic Fe_3Si (and possibly a small fraction of Fe nanoparticles) in the SiC matrix. We find a wide range of blocking temperatures, T_B, which start from 400 K for a dose of 2.0×10^{16} cm^{-2}, and shift downwards to ~220 K for 3.0×10^{16} cm^{-2}. For the lowest dose of 1.0×10^{16} cm^{-2} at 200 keV, we find evidence of ferromagnetism below 20 K via weak magnetic hyperfine interaction. Our measurements suggest that for a maximum Fe concentration in the range of 1–3%, which corresponds to this lowest Fe dose, the possibility exists to obtain a DMS in Fe-implanted SiC, prepared at lower or equal implantation doses.

1. Introduction

Exploiting the spin in addition to the charge of the electron provides new functionality to microelectronic devices. In order to produce magnetic materials with highly spin polarized electrons, many efforts have concentrated on preparing diluted magnetic semiconductors (DMSs) in which transition metal atoms are introduced into the semiconducting host lattice [1].

The high spin polarization is caused by the exchange interaction between the sp band electrons and the d electrons associated with the localized moment of the transition metal (e.g. Mn^{2+}) resulting in extremely large Zeeman splittings of the electronic levels. They are promising candidates for efficient spin injection into semiconducting materials in order to fabricate spin-FETs (field effect transistors) and related devices [2]. For example, attempts at electrical and optical spin injection have been made involving GaMnAs, GaMnN, ZnMnSe and CdMnTe [3–9]. The most striking advantage of these materials, in favour of ferromagnetic metal contacts, is the absence of the resistivity mismatch problem [10] which has to be overcome in the case of metal contacts either by tunnelling barriers or highly doped Schottky barriers [11–19]. Recently, successful spin injection at room temperature (RT) from an epitaxially grown Fe_3Si layer onto GaAs was demonstrated [20]. This is an example of a Heusler-like alloy (Fe_2FeSi) ferromagnet and a possible half-metal (still not confirmed), which is a favourable case for spin injection. The experiments in [20] yielded a transport spin polarization of $P = 45\%$ by the Andreev reflection method.

For practical applications DMSs with Curie temperatures T_C above RT are needed. The problem is to incorporate as much of the transition metal atom into the host matrix as is necessary to obtain ferromagnetism at and above RT. While for II–VI semiconductors doping is not problematic, the solubility limit of III–V semiconductors for the doping materials is rather low. One possible route to overcome this problem is to work far from equilibrium and use low-temperature molecular beam epitaxy (MBE). In this way one of the first III–V DMSs, InMnAs, which exhibited a very low T_C was grown in 1989 [21]. The first DMS based on GaAs was grown by Ohno [22] in 1996, and at this time T_C was limited to 60 K. To the best of our knowledge, the current record is 159 K [23], which is still far below RT. After the work by Dietl *et al* [24], which emphasized the importance of hole-mediated ferromagnetism and predicted high Curie temperatures for wide band gap semiconductors like GaN or ZnO, many experimentalists focused their work on these or similar compounds [25–28]. As for GaN, Sasaki *et al* [29] found Curie temperatures above 740 K for 3% Mn doping of GaN which was produced by MBE on Al_2O_3. EXAFS (extended x-ray absorption fine structure) and RBS (Rutherford backscattering) studies showed that the Mn was substituting for the Ga sites and was distributed uniformly. Kuwabara *et al* [30] used Fe as well as Mn, both at 2% doping level, again for GaN on Al_2O_3, but identified Fe clusters by electron microscopy and superparamagnetic behaviour by superconducting quantum interference device (SQUID) magnetometry. For Mn, the electron microscope showed a homogeneous matrix and the magnetic behaviour was paramagnetic. Finally, Ploog *et al* [31] produced GaMnN on 4H-SiC by MBE and observed no precipitates for 7.6% Mn, but found an insulating spin glass behaviour below 10 K. For 13.7% Mn, manganese-rich clusters were formed and the behaviour above RT was ferromagnetic.

Little attention has been paid so far to the wide band gap semiconductor silicon carbide (gap energy $E_g = 3.0$ eV for 6H-SiC modification) despite its potential for high-power and high-temperature electronics and its excellent transport properties and dopability. A theoretical study [32] showed that Cr and Mn in 3C-SiC produce a ferromagnetic solid solution at both the Si and C sites, but with different magnetic moments. Fe behaves differently, for in 3C-SiC it remains paramagnetic, but Fe on the Si site within the 6H-SiC modification leads to ferromagnetic ordering at low concentrations (2%) with a magnetic moment of 2.76 μ_B per Fe atom [32]. This behaviour is confirmed theoretically in another work [33], which deals with the cubic 3C-SiC modification, but performs calculations for all the transition metals from Sc to Zn. Considering the problem of compound formation, an XAS (x-ray absorption spectroscopy) study on ion-implanted SiC with Fe, Ti or Co with concentrations of 10% over a depth of 50–60 nm at the K-edge of the implanted ion indicated that Co forms CoSi, whereas for iron

Table 1. The first column specifies the sample labels for both n- and p-type samples. Second column: ^{57}Fe dose. Third column: maximum ^{57}Fe concentration in the depth profile. Fourth column: implantation energy E. Fifth column: observed blocking temperature T_B.

Sample no	^{57}Fe dose (10^{16} cm^{-2})	Max. ^{57}Fe conc. (at.%)	E (keV)	T_B (K)
p1, n1	0.55	1.1	100	—
p2, n2	1.0	2.1	100	—
p3, n3	2.0	4.6	100	p3: >400
p-hd	20	27.6	100	—
p4, n4	1.0	1.2	200	n4, p4: ∼20
p5, n5	3.0	3.8	200	p5: ∼220

Fe clusters and FeSi coexist, and Ti forms TiC [34]. Theodoropoulou *et al* [35, 36] used ion implantation of Mn, Fe and Ni ions and achieved T_C values of 270 K for 5 at.% implanted 6H-SiC samples, excluding the Ni implantation which resulted in paramagnetism. 3 at.% doping levels led to paramagnetic behaviour in all cases. No secondary phases could be detected in both cases by selected area diffraction pattern (SADP) analysis and transmission electron microscopy (TEM) [35, 36].

The present work reports on the structural and magnetic investigations of ^{57}Fe-implanted 6H-SiC wafers, mostly p-type. ^{57}Fe conversion electron Mössbauer spectroscopy (CEMS) [37] was employed for the study of the local environment of the ^{57}Fe nucleus in the SiC matrix. By the hyperfine interactions of the ^{57}Fe nucleus with its surroundings one obtains valuable information about its local symmetry and about both the charge and the magnetic state of the Fe atom [38]. The CEMS measurements were correlated with structural investigations by x-ray diffraction (XRD) analysis, depth-selective Auger electron spectroscopy (AES), TEM and superconducting quantum interference device (SQUID) magnetometry. It will be shown that the formation of the compound Fe_3Si is the main reason for ferromagnetic properties of the Fe-implanted SiC.

2. Experimental details

Polished and clean single crystals of the 6H-polytype of α-SiC with (0001) orientations (obtained from Cree Corp., USA) were implanted at energies of 100 or 200 keV with a high-current implanter model DANFYS 1090 from Danfysk (Jyllinge, Denmark). All crystals were of the same size of 10×10 mm^2. The implanted area was the same for all samples. The substrate temperature during implantation was held at 350 °C in order to minimize amorphization. Four different doses of ^{57}Fe and two implantation energies were employed, as indicated in table 1, with the notation 'n' for n-type and 'p' for p-type samples. One p-type sample was implanted with a particularly high dose of 2×10^{17} ions cm^{-2} (sample p-hd) (hd: high dose). In the present paper we are dealing mostly with the properties of the p-type samples ($p \approx 3.2 \times 10^{18}$ cm^{-3}). The ^{57}Fe-concentration depth profile was measured by sputter-AES on n-type samples only, because we think that the Fe-implantation profile is not affected by the type of doping. All measurements, except SQUID and TEM, were carried out directly after implantation and after rapid thermal annealing (RTA). RTA was performed under Ar atmosphere at 1000 °C for 2 min, using a halogen lamp. Throughout the paper, when we mention annealing, we mean always RTA. Both SQUID and TEM measurements were performed only on the annealed samples. The depth profile of the ^{57}Fe atoms was determined by the sputter-Auger method with a Microlab 310F from Fisons. Sputtering was done with 3 keV Ar ions, a current density of 1 μA mm^{-2},

and sputtering rates of about 0.3 nm s^{-1}. X-ray diffraction patterns were recorded in θ–2θ geometry with the PW1349/30 model from Philips. For CEMS at RT, a homemade He–CH_4 proportional counter was used, with the sample mounted inside. The 4.2 K CEM spectra were obtained with a channeltron electron detector placed, together with the sample, in the inner chamber of a liquid-He bath cryostat. A Mössbauer drive system operating in constant acceleration mode with conventional electronics and a ^{57}Co source (embedded in a Rh matrix) were employed. The 14.4 keV γ-radiation was at perpendicular incidence with respect to the sample plane. The CEM spectra were least-squares fitted using the NORMOS program package developed by Brand [39]. All isomer shifts are given relative to α-Fe at RT.

3. Results and discussion

3.1. X-ray analysis, transmission electron microscopy (TEM)

θ–2θ x-ray diffraction (XRD) scans for the as-implanted and annealed (RTA) samples were performed over an angular range of 20°–120°. The as-implanted samples showed no extra peaks compared to a non-implanted piece of SiC from the same batch, which we used as a reference (figure 1(a)). After annealing, two samples exhibited a broad extra peak, at 44.81° (sample p3) and 45.03° (sample p5), with a FWHM of more than 2°, which is identified as the (220) reflection of the Fe_3Si crystal structure (figure 1(b)). The as-implanted high-dose sample, p-hd, showed reflections at 45.26° and 100.52°, which were indexed as the (220) and (440) reflections of Fe_3Si (figure 1(c)). Here, the FWHM of the (220) peak is three times smaller than the width of the (220) peak for the low-dose implanted samples. The (220) and (440) peaks are fundamental reflections of the Fe_3Si structure ($h + k + l = 4n$, n non-zero integer) [40]. We would like to mention that the Bragg peaks observed here also might originate from bcc Fe, since the lattice parameter of Fe_3Si is about twice as large as that of bcc Fe. However, the small positive isomer shift values observed at RT in the Mössbauer spectra (see section D) indicates the predominant presence of Fe_3Si rather than α-Fe. The superlattice reflections due to the $D0_3$ structure of chemically ordered Fe_3Si (values h, k, l are all odd) are absent. Also the superlattice reflections for the B2 structure of Fe_3Si (all values h, k, l even and $h + k + l = 4n + 2$, n integer including zero) are missing. Applying the Debye–Scherrer formula for the relation between the particle size and the FWHM one obtains average particle diameters of the Fe_3Si phase of 3.3, 3.4 and 12.1 nm for samples p3, p5 and p-hd, respectively. The occurrence of only one type of reflection provides evidence for an epitaxial relationship of the Fe_3Si nanoclusters with the SiC matrix, i.e. the Fe_3Si lattice is coherent with the SiC lattice. Furthermore, the samples with the smallest particle sizes have slightly larger lattice parameters than bulk Fe_3Si with a value of 0.566 nm [41], namely 0.570 nm for p3 and 0.572 nm for p5.

Cross-sectional TEM micrographs of sample p3 (after thermal annealing), with an implantation dose of 2×10^{16} cm^{-2}, are shown in figure 2. The overview in figure 2(a) exhibits three different regions. Starting from the surface (at the top of figure 2(a)) one observes the implanted region up to a depth of ∼100 nm, which has its maximum ^{57}Fe concentration at a depth of ∼40 nm below the sample surface (figure 3(a)). The crystallinity of this region is clearly visible. The following range, starting at a depth of ∼100 nm (dark contrast) apparently is amorphous, and, finally, one arrives at the crystalline underlying substrate. The inset in figure 2(a) shows a magnification of the crystalline region, and one can observe a distribution of small (upper part of the inset) and large (lower part of the inset) clusters. The contrast was inverted in order to obtain a better visibility. The high-resolution picture (figure 2(b)), taken from a depth of about 50 nm below the surface, clearly displays small crystalline clusters of average sizes smaller than 5 nm, which are epitaxially embedded in the SiC substrate. The

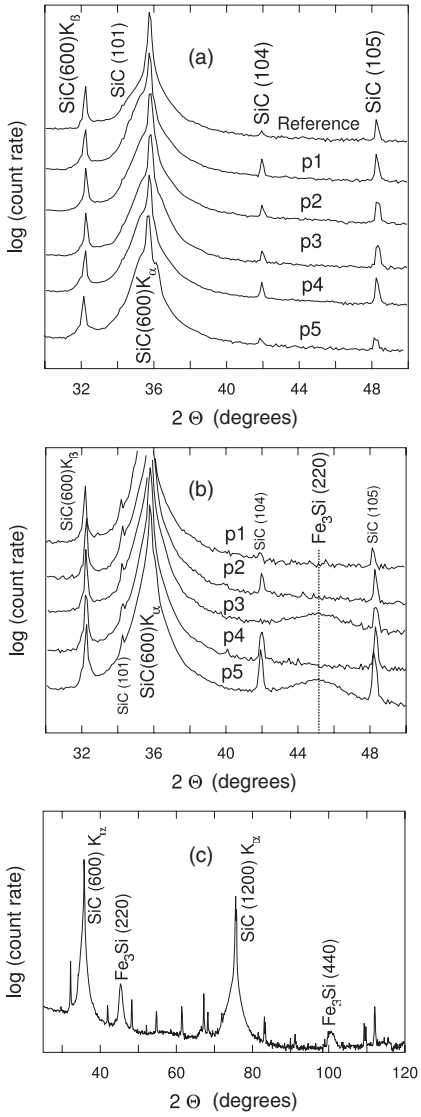

Figure 1. (a) θ–2θ x-ray diffraction scans of as-implanted samples p1, p2, p3, p4, p5 ('Reference' depicts a non-implanted SiC wafer), (b) samples after RTA at 1000 °C for 2 min under Ar atmosphere, (c) as-implanted high-dose sample p-hd (Cu Kα radiation).

evaluated lattice parameters of these particles ranged from 0.204–0.210 nm. These values can be compared with α-Fe in (110) orientation (0.2027 nm), γ-Fe in (111) orientation (0.2072 nm) or Fe_3Si in (220) orientation (0.2001 nm). The possible formation of the carbide Fe_3C can be excluded due to the different lattice parameter [42].

3.2. Sputter-Auger depth profiling

In order to study the distribution of the ^{57}Fe atoms in the SiC matrix after both implantation and RTA, we employed the sputter-AES method. Typical depth profiles obtained are presented

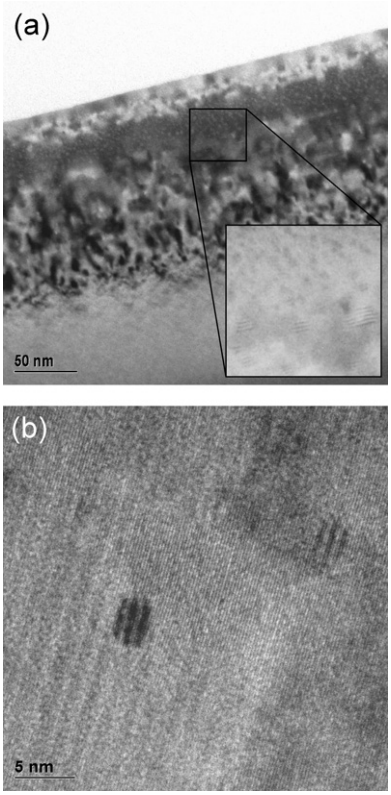

Figure 2. Cross-sectional TEM micrographs of sample p3, implanted with 2×10^{16} ^{57}Fe ions cm^{-2}, after RTA. (a) Overview with the sample surface at the top of the picture. Three main regions are visible: the first region to a depth of about 100 nm includes the maximum ion concentration and shows a recrystallized region; the second (dark) part consists of amorphous material; the third part is the underlying substrate which remained crystalline. The inset (inverted contrast) shows a magnified region with a typical depth dependence of the size distribution of nanocrystalline grains. (b) High-resolution micrograph in a depth of 40–50 nm. Small, epitaxial grains of 50 Å diameter are visible.

in figure 3. Only the n-type samples have been investigated. The general observation was that in all samples, except for sample n2, the concentration profile after annealing was shifted towards the sample surface (figure 3) with respect to the as-implanted case. This shift was found to be nearly independent of implantation dose and energy and had a mean value of 20 nm. The maximum ^{57}Fe concentration and the width of the implantation profiles are only slightly reduced after annealing (estimated from fitting Gaussians to the data). Regarding the diffusion coefficients of different dopants in SiC, which are several orders of magnitude lower than in Si [43], the diffusion of larger atoms in SiC is nearly negligible. Smaller atoms migrate mainly via the interstitial mechanism, while larger atoms diffuse via silicon or carbon vacancies. Since the covalent radius of iron is 0.117 nm and that of silicon is 0.111 nm the most probable mechanism for diffusion of Fe in SiC is by silicon vacancies which are produced during implantation. A model proposed for boron diffusion in SiC [44] describes the migration of the boron atoms via the kick-out mechanism (a substitutional boron is kicked out from the lattice site by interstitial silicon resulting in interstitial boron). This mechanism is also observed in silicon and is thought to apply also in the case of Fe diffusion. In the irradiated

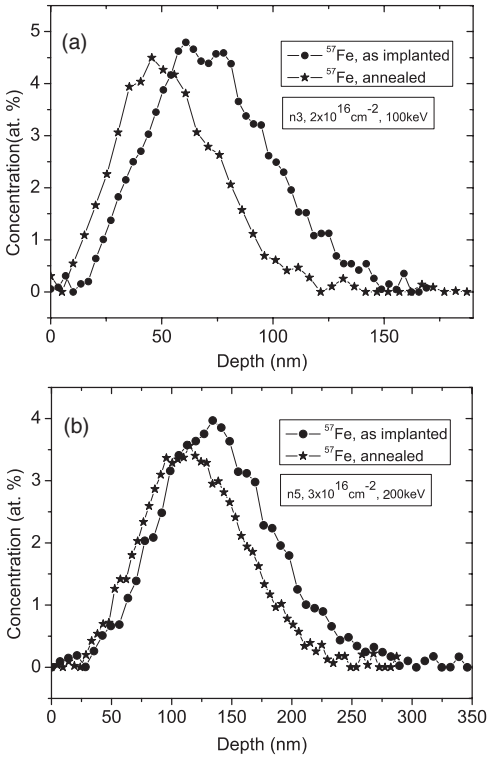

Figure 3. Depth profiles of ^{57}Fe concentrations for (a) sample n3 (2×10^{16} ions cm^{-2}, 100 keV) and (b) sample n5 (3×10^{16} ions cm^{-2}, 200 keV). Full circles: directly after implantation. Asterisks: after rapid thermal annealing (RTA).

region the distribution of carbon and silicon interstitials is disturbed and, due to the heavier mass of silicon, excess silicon is accumulated in the region closer to the surface. By annealing, these interstitials become highly mobile and enhance the diffusion of Fe towards the surface, which is an explanation for the observed shift of our implantation profiles. Since the measured Si concentration (not shown) in the implanted regions was reduced more strongly than the measured carbon concentration (not shown) already before the annealing, this provides an additional argument for the conclusion that iron preferably substitutes for Si from the beginning (as-implanted state) which is also consistent with the different formation energies of Si-site and C-site doping [45].

3.3. Magnetometry

As-implanted samples have not yet been investigated by SQUID magnetometry. Here we concentrate on the samples after RTA. In order to estimate the magnetic ordering temperatures of our samples, T-dependent zero-field-cooled (ZFC) and field-cooled (FC) magnetization curves were taken on samples n4, p3 and p5 after RTA. The results are shown in figures 4(a), (b), (c), respectively. For the SQUID measurements samples of the same size were used. The implanted regions had almost the same surface area for all samples. The hysteresis loops shown in figure 5 were obtained after subtraction of the linear background from the non-implanted SiC substrate. Samples n4, p3 and p5 were zero-field cooled from 400 K to 30 K, 20 K and 5 K

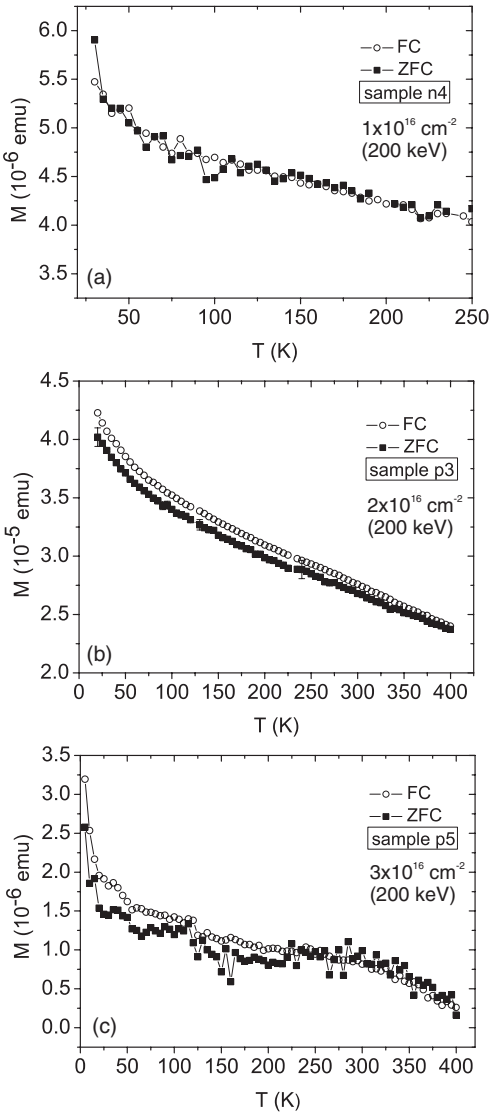

Figure 4. Temperature dependence of the zero-field-cooled (ZFC, full squares) and field-cooled (FC, open circles) magnetization curves for samples n4 (a), p3 (b) and p5 (c) after RTA. A field of 2000 Oe was applied in the sample plane for cooling and measurement.

respectively. The ZFC and FC magnetization measurements were performed in an external field of 2000 Oe by heating the samples up to 400 K (ZFC) followed by recooling to the same temperature (FC). The ZFC–FC curves of sample n4 (figure 4(a)) are overlapping, even at the lowest temperature. Taking into account the vanishing coercive field at the low temperature of 20 K (figure 5(a1)) one can conclude that sample n4 consists of tiny superparamagnetic particles above their blocking temperature, T_B, which lies at $\sim$20 K or below. Figure 5(a2) shows the hysteresis loop for sample p4 at 20 K. No convincing coercive field can be claimed because of the weakness of the signal and large scatter of the data points. This demonstrates that sample p4 also consists of tiny superparamagnetic particles with $T_B \leqslant 20$ K, similar to sample n4. Both

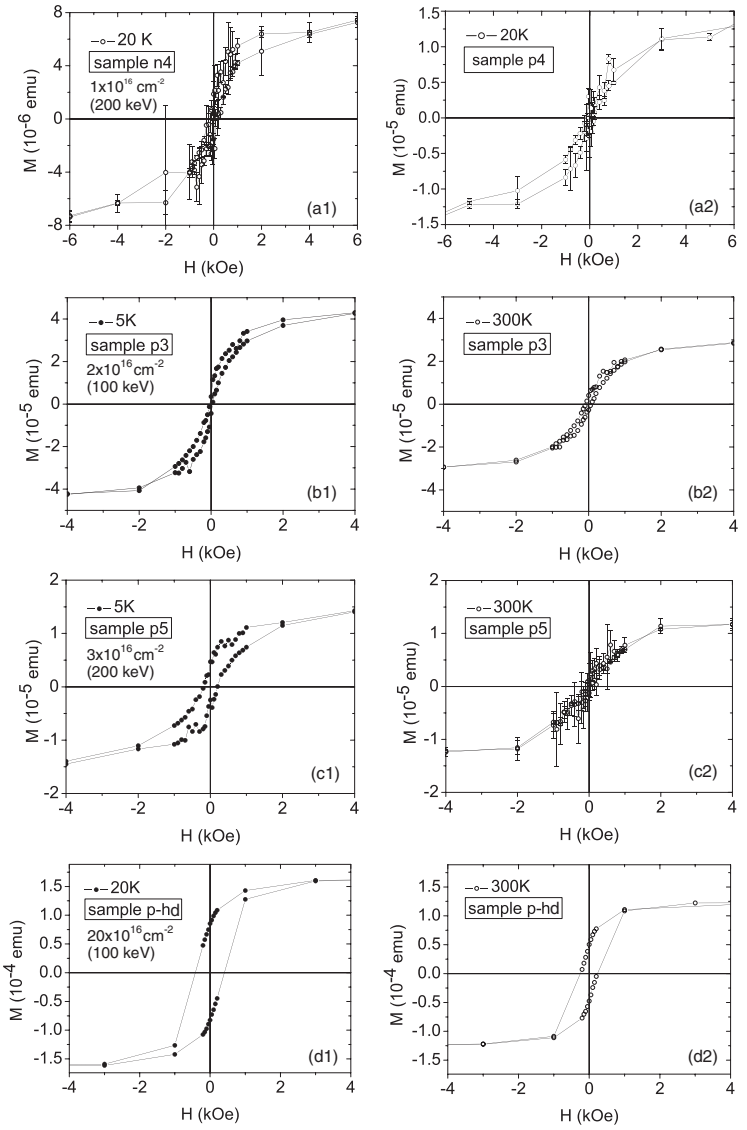

Figure 5. Magnetic hysteresis loops taken at low temperatures ((a1), (a2), (b1), (c1), (d1)) and at 300 K ((b2), (c2), (d2)) for samples n4, p4, p3, p5 and p-hd, respectively. (All measurements were done after RTA.)

magnetization curves in figures 5(a1) and (a2) are S-shaped, which is also a typical sign of superparamagnetism. Since there is no splitting of the ZFC–FC curves, observed in figure 4(a), one has further information about missing long-range ferromagnetic order in sample n4 for $T \geqslant 30$ K.

By contrast, the FC–ZFC branches in figure 4(b) for sample p3 are observed to diverge. One can notice that even at 400 K their difference is non-zero (the error bars are of smaller size than the symbols), and, consequently, $T_B > 400$ K. This agrees with results of figures 5(b1) and (b2), where the hysteresis loops at 5 and 300 K, respectively, of sample p3 exhibit measurable coercive fields ($H_C \approx 42$ Oe at 5 K and 69 Oe at 300 K). This means that there are

larger particles in sample p3 which are below their blocking temperature. The conclusion is that we have a large particle size distribution in sample p3, as can also be seen from TEM (see inset in figure 2(a)). The larger particles behave ferromagnetically below ∼400 K. For sample p5, the apparent intersection of the two magnetization curves occurs at about $T_B \approx 220$ K (figure 4(c)). This is due to a presumed sharper particle size distribution and smaller particles than in sample p3. The value of $T_B = 220$ K agrees with the result of figures 5(c1) and (c2), where a hysteresis loop and a coercive field of $H_C \approx 198$ Oe is observed at 5 K, but not at 300 K, which is well above $T_B \approx 220$ K. Regarding the magnetization loops of the high-dose sample p-hd at 20 and 300 K (figures 5(d1) and (d2)), one observes at 20 K and even at RT a pronounced hysteresis with a large coercive field ($H_C = 408$ Oe at 20 K and $H_C = 236$ Oe at RT). In connection with the x-ray diffraction pattern of this sample (figure 1(c)) it is very likely that here there are no small grains, but rather an extended coherent phase of Fe_3Si has formed. This assumption is supported by the sharpness of the Fe_3Si diffraction peaks in the XRD pattern of sample p-hd (figure 1(c)) as compared to the very broad Fe_3Si peaks for samples p3 and p5 (figure 1(b)). The implication for sample p-hd is that its hysteresis loops originate from domain wall motion and pinning, whereas for samples p3 and p5 the hysteresis observed at low T reflects the finite magnetic anisotropy constant of blocked single-domain superparamagnetic particles. Apart from these conclusions one may also notice the outwardly concave behaviour and the non-saturation behaviour of the ZFC–FC magnetization at low temperature (figures 4(b) and (c)) which is different from the usual behaviour of superparamagnetic nanoparticles [46]. Assuming that, apart from the obvious Fe_3Si contribution to the sample magnetization, a second contribution plays a role, which arises from the local exchange coupling of small Fe_3Si clusters (and presumably of the iron atoms on substitutional Si lattice sites) via the charge carriers of the SiC matrix, the observed magnetization shapes are reasonable, since DMS systems (as we deliberately assume also in our case) always exhibit a non-mean-field-like T-dependence of the magnetization [47, 48]. The missing convex part of sample p3 (figure 4(b)) may result from the fact that its T_C lies much above 400 K (the maximum attainable temperature for the magnetometer). The exact form of the magnetization curves depends on the density ratio of the holes to the local moment density (Fe atoms), and whether the carriers are non-degenerate (isolating systems) or degenerate (metallic systems) [47, 48]. Since we did not perform electrical measurements on our samples, we cannot distinguish between these two cases.

3.4. Mössbauer spectroscopy (CEMS)

3.4.1. Implantation dose $\geqslant 2 \times 10^{16}$ ions cm^{-2}. CEM spectra obtained on as-implanted or annealed samples p3 and p5 in perpendicular geometry at RT and in zero external field are shown in figure 6. Figure 7 exhibits the CEM spectra of sample p4 at 4.2 K. The corresponding Mössbauer spectral parameters for all samples are presented in table 2. Since there was no obvious magnetic hyperfine splitting at RT (except for sample p-hd, as seen in figure 8(a)), a distribution $P(QS)$ of quadrupole-split doublets was used to fit the data in figure 6. In order to obtain a good fitting a linear correlation between quadrupole splitting QS and isomer shift δ had to be assumed, as is often the case in disordered solids [49]. The fitting procedure reflects the already introduced feature that our samples are composed of a size distribution of superparamagnetic particles. Depending on the size and composition of a certain particle, the ^{57}Fe atoms in the outer shell of a particle perceive different symmetries and numbers of neighbours of Si, C, or Fe atoms. This leads to a distribution of quadrupole splittings and isomer shifts originating from the particle shell. The net result is an asymmetric doublet. Thus the extracted distributions of quadrupole splittings, $P(QS)$, are broad and are extending from zero to rather high values of ∼2.5 mm s^{-1}. This broad QS range reflects the structural

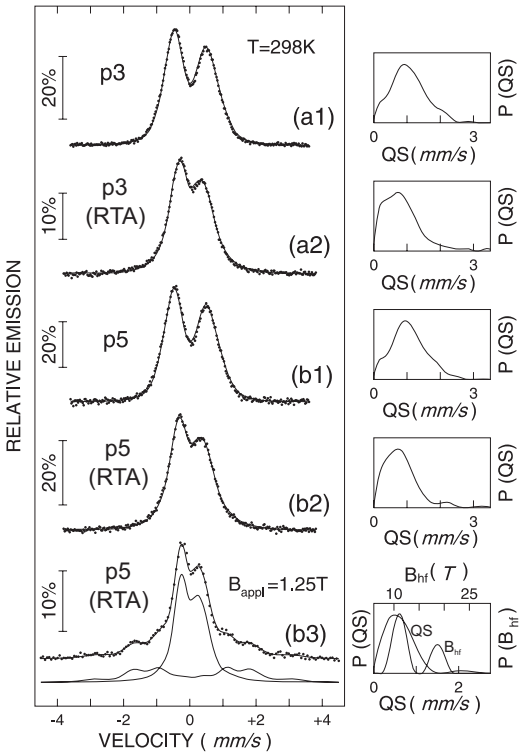

Figure 6. Conversion electron Mössbauer (CEM) spectra measured at room temperature on samples p3 and p5, implanted with 2×10^{16} and 3×10^{16} ions cm^{-2}, respectively. (a1), (b1) As-implanted state. (a2), (b2) After RTA. (b3) After RTA, with an applied field of 1.25 T. The spectra were least-squares fitted with a distribution of quadrupole splittings, $P(\mathrm{QS})$, and, for (b3), with both $P(\mathrm{QS})$ and a magnetic hyperfine field distribution $P(B_{\mathrm{hf}})$, as shown on the right-hand side.

inhomogeneity observed by TEM in figure 2(a). Further the ^{57}Fe concentration profile (figure 3) results in a distribution of local neighbourhoods of Fe atoms (also in the core of the particles), which in addition to the effect of the particle size distribution contributes to the distribution $P(\mathrm{QS})$. The $P(\mathrm{QS})$ results at RT for our as-implanted samples are almost the same as in the work of McHargue and Horton [51, 52], although the samples in [48] and [49] were implanted at RT (our samples were held at an elevated temperature of 350 °C during implantation) and no annealing procedure was applied afterwards.

One can notice in table 2 that the average isomer shift $\langle\delta\rangle$ of all samples at RT is positive and relatively small (about 0.12–0.13 mm s^{-1}). This value suggests the existence of the metallic Fe^0 state as in Fe_3Si [57]. On the other hand, Fe^{II} or Fe^{III} valence states, both in low-spin states, with $S = 0$ for Fe^{II} or $S = 1/2$ for Fe^{III}, also show similarly small isomer shifts (S is the total spin angular momentum of the Fe atom) [50]. The average quadrupole splittings of $\langle\mathrm{QS}\rangle = 1.0$–$1.2$ mm s^{-1} show nearly no or only weak temperature dependence (see table 2), which is typical for metallic Fe^0 systems or for the low-spin Fe^{II} state. The Fe^{II} state in its t_{2g}^6 configuration has no intrinsic valence contribution to the electric field gradient (EFG) and shows a nearly temperature-independent quadrupole splitting only due to the lattice contribution to the EFG. On the other hand, the t_{2g}^5 configuration of low-spin Fe^{III} shows appreciable thermal population of closely spaced low-lying excited electronic levels when the neighbourhood is slightly distorted from cubic symmetry, and, therefore, a strong temperature

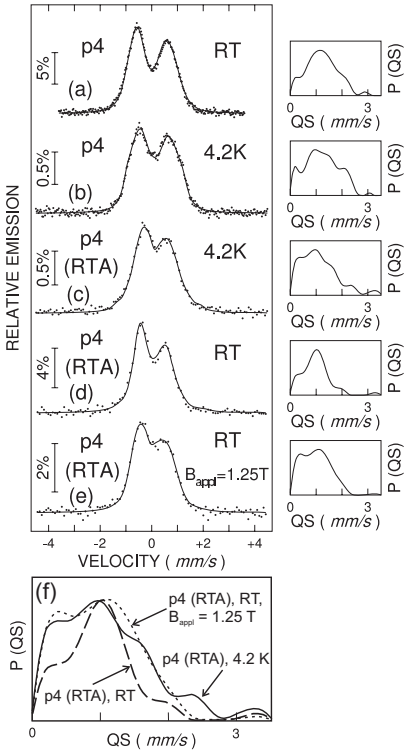

Figure 7. CEM spectra of sample p4 measured at 4.2 K or RT. (a) As implanted state, T = RT (b) as-implanted state, $T = 4.2$ K, (c) after RTA, $T = 4.2$ K, (d) after RTA, T = RT, (e) after RTA at RT with an applied field of 1.25 T. The spectra were least-squares fitted with a distribution of quadrupole splittings P(QS), right-hand side. (f) Comparison of P(QS) for sample p4 (after RTA) at RT in zero applied field (long dashed curve), at RT with an applied field of 1.25 T (short dashed curve), and at 4.2 K in zero applied field (full curve).

dependence of the quadrupole splitting would appear [50]. Implanting with higher doses or annealing the samples results in a reduction of the quadrupole splittings (figures 6(a2), (b2) and table 2); the isomer shifts, however, are not affected by the annealing. This indicates that the symmetry around the Fe atoms is higher after annealing, but the charge state remains the same. As a conclusion we can say from the isomer shift and the weak T-dependence of $\langle$QS$\rangle$ that the most probable valence state in our samples is that of the metallic Fe^0 state.

The asymmetry in the line intensity of the quadrupole-split spectra, which we ascribe to a correlation of QS and δ and which is observed before and after annealing, could possibly be due to crystallographic texture, which may cause a preferred direction of the main component, V_{zz}, of the electric field gradient (EFG tensor). In order to check for texture effects, we have performed angular dependent CEMS experiments at RT for the annealed sample p5 (not shown here) and used two broad Lorentzian lines for fitting the doublet. In this experiment no change was observed in the intensity ratio of the left line to the right line of the doublet for different angles of incidence of the gamma-ray with respect to the sample plane (90°, 70°, 50°, 30°). Therefore the effect of texture can be excluded, and the V_{zz} directions are randomly oriented. Since we observe a blocking temperature of 220 K for sample p5 (see figure 4(c)), which is below the Curie temperature T_C of the individual particles, we can conclude that the doublet at RT originates from superparamagnetic Fe atoms which are located in the core of

Table 2. Mössbauer spectral parameters at room temperature (RT) and at 4.2 K obtained by least-squares fitting the CEM spectra of samples p1, p2, p3, p4 and p5 with a distribution of quadrupole-split doublets. In case of samples p3 and p5 at 4.2 K, where magnetically split sextets in addition to a central quadrupole doublet appear, the Mössbauer parameters given here refer to the quadrupole doublet only. $\langle\delta\rangle$ = average isomer shift relative to α-Fe at room temperature, $\langle$QS$\rangle$ = average quadrupole splitting. (RTA = rapid thermal annealing).

	p1	p2	p3	p4	p5
T = RT, as implanted					
$\langle\delta\rangle$ (mm s^{-1})	0.12(3)	0.12(4)	0.13(3)	0.12(3)	0.13(3)
$\langle$QS$\rangle$ (mm s^{-1})	1.254(6)	1.175(8)	1.060(4)	1.233(6)	1.069(6)
T = 4.2 K, as implanted					
$\langle\delta\rangle$ (mm s^{-1})	—	—	0.23(4)	0.21(2)	0.24(3)
$\langle$QS$\rangle$ (mm s^{-1})	—	—	1.110(8)	1.229(8)	1.118(6)
T = RT, RTA					
$\langle\delta\rangle$ (mm s^{-1})	0.13(6)	0.14(5)	0.15(4)	0.15(7)	0.15(5)
$\langle$QS$\rangle$ (mm s^{-1})	1.129(9)	0.934(9)	0.876(6)	1.01(1)	0.848(7)
T = 4.2 K, RTA					
$\langle\delta\rangle$ (mm s^{-1})	—	—	—	0.25(3)	—
$\langle$QS$\rangle$ (mm s^{-1})	—	—	—	1.12(1)	—

superparamagnetic Fe_3Si particles with varying composition and possibly a distorted lattice and/or in the outer (lattice-distorted) shell of such Fe_3Si particles, sensing a less symmetric (non-cubic) local environment and a spatial distribution of surroundings (indicated by the line broadening). We cannot exclude that a small fraction of superparamagnetic (lattice-distorted) bcc-Fe particles also contribute to P(QS). By rotating the sample relative to the γ-ray direction the apparent intensity ratio of the two lines of the doublet is not changing because the distribution P(QS) itself effectively remains the same.

A direct proof of the superparamagnetism in sample p5 is given in figure 6(b3). Figure 6(b3) shows the CEM spectrum of sample p5 at RT after RTA, with an applied field $B_{\rm appl}$ of 1.25 T. It was fitted with two spectral components: a quadrupole distribution P(QS) for the central asymmetric quadrupole split feature, and an effective magnetic hyperfine field distribution $P(B_{\rm hf})$ for the wings at higher velocities. Since the maxima (observed in $P(B_{\rm hf})$) are located at effective hyperfine fields of 10.8 and 18.8 T, which are clearly larger than the applied field, this result definitely proves that at RT a certain fraction of ^{57}Fe atoms in sample p5 (30%, according to the relative spectral area of $P(B_{\rm hf})$) is located in larger superparamagnetic particles whose superparamagnetic relaxation is slowed down or blocked by the applied field. (The magnetization of the residual fraction of ^{57}Fe atoms (70%) in smaller particles still fluctuates rapidly within the Mössbauer timescale resulting in the central quadrupole doublet.) Because they are small single-domain particles their magnetic easy axes orientations are separated by a magnetic anisotropy barrier U. Superparamagnetic relaxation occurs when the barrier U can be overcome by thermal energy, and when the associated relaxation time is much faster than the Larmor precession period of the ^{57}Fe nuclear moment, resulting in the central quadrupole doublet. The applied magnetic field prevents the thermal relaxation of the particle magnetization above their anisotropy barriers and effectively pushes $T_{\rm B}$ for the larger particles above RT. Therefore, sample p5 is clearly in the superparamagnetic state at RT and zero external field. This supports our SQUID result for sample p5 which indicates $T_{\rm B}$ = 220 K.

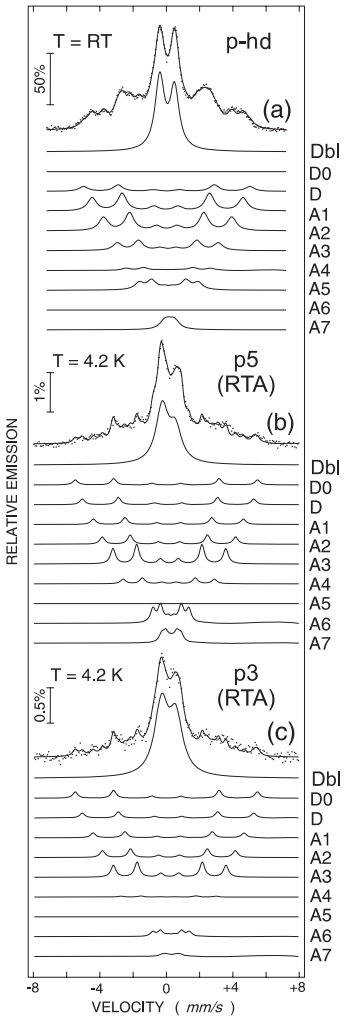

Figure 8. CEM spectra of those samples after RTA which show a magnetic hyperfine splitting: sample p-hd at RT (a), and samples p5 (b) and p3 (c) at 4.2 K. The least-squares fits were performed with ten subspectra: a central asymmetric quadrupole doublet (Dbl) for a non-magnetic phase, and nine magnetically-split sextets (D0, D, A1–A7) for atomically disordered Fe_3Si.

3.4.2. Implantation dose 1×10^{16} ions cm^{-2}. For samples p4 and n4, according to figures 1(a) and (b), no Fe_3Si nanoparticles were detectable by XRD. Further, similar hysteresis loops were observed at 20 K for sample p4 (figure 5(a2)) and sample n4 (figure 5(a1)). One should notice that both samples, p4 and n4, had the same low dose of 1×10^{16} ^{57}Fe cm^{-2} at 200 keV. Clearly, both samples (after RTA) are not ferromagnetic but superparamagnetic at 20 K, according to the SQUID magnetization observed in figures 5(a1) and (a2). Zero-field CEM spectra of sample p4, after implantation (figures 7(a) and (b)) and after RTA (figures 7(c) and (d)), do not show a resolved magnetic hyperfine splitting, even at 4.2 K (figures 7(b) and (c)), but an apparent broad distribution $P(\mathrm{QS})$ of quadrupole splittings. Further, an applied magnetic field B_{appl} of 1.25 T with sample p4 at RT did not produce a visible magnetic splitting (figure 7(e)) that would hint to superparamagnetism, contrary to sample p5 (figure 6(b3)). This proves that sample p4 (after

RTA) is paramagnetic at RT. However, the quadrupole distribution $P(\mathrm{QS})$ of sample p4 at 4.2 K exhibits distinct features (shoulders) (figures 7(b) and (c), right-hand side) which are absent at RT (figures 7(a) and (d)), and are not found for samples p3 and p5 at RT (figure 6). Furthermore, there is a slightly larger increase of the average quadrupole splitting $\langle \mathrm{QS} \rangle$ of 0.11 mm s^{-1} by cooling sample p4 (RTA) from RT to 4.2 K (table 2), as compared to the other samples. Both observations could be an indication for the presence of a small magnetic hyperfine splitting due to magnetic ordering, in addition to the stronger electric quadrupole interaction, in sample p4 at 4.2 K after RTA. In the following we will discuss this aspect further.

In figure 7(f) we compare the apparent distribution of quadrupole splittings, $P(\mathrm{QS})$, of sample p4 (after RTA) at RT and 4.2 K in zero external field, and at RT in an applied field of 1.25 T. In comparison to $P(\mathrm{QS})$ in zero field at RT, the probability $P(\mathrm{QS})$ in zero field at 4.2 K shows a drastic increase at low and high QS values. This is also reflected in the increase of the corresponding distribution width (FWHM) from $\Delta\mathrm{QS} = 0.84$ mm s^{-1} at RT to $\Delta\mathrm{QS} = 1.65$ mm s^{-1} at 4.2 K. While the increase of $P(\mathrm{QS})$ at high QS values could be explained by the usual increase of quadrupole splittings by lowering the temperature (though small in the metallic Fe^0 and Fe^{II} state, as mentioned before), the strong increase at low QS values (including $\mathrm{QS} \approx 0$ mm s^{-1}) cannot be understood by this mechanism, because this would mean a reduction of QS for some of the Fe species at low T, which is not physically sound. Therefore, another mechanism must be responsible for the $P(\mathrm{QS})$ increase at low QS values combined with the $P(\mathrm{QS})$ increase at high QS values, if T is reduced to 4.2 K. The only reasonable explanation of this effect is the development of a weak magnetic hyperfine interaction at 4.2 K, combined with the existing larger quadrupole interaction. It is well known for ^{57}Fe that the lines of a quadrupole-split doublet broaden under the action of a weak magnetic field (external or hyperfine field) due to the fact that the additional Mössbauer lines resulting from the weak Zeeman interaction involved cannot be resolved [53]. This is what is observed in the spectrum of sample p4 (RTA) at RT and the corresponding $P(\mathrm{QS})$ distribution (figure 7(e)), when a weak field of 1.25 T is applied: the doublet lines are broadened as compared to the zero-field case (figure 7(d)), and the dip near zero velocity between the two doublet peaks almost disappears. As a consequence, as is observed in figure 7(f), the probability $P(\mathrm{QS})$ at $B_{\mathrm{appl}} = 1.25$ T increases at low and high QS values as compared to the zero-field case, leading to a drastic broadening of $P(\mathrm{QS})$ towards a width $\Delta\mathrm{QS}$ of 1.7 mm s^{-1}. Now we compare the two distributions $P(\mathrm{QS})$ for sample p4 (RTA) at 4.2 K in zero external field and at RT in $B_{\mathrm{appl}} = 1.25$ T (figure 7(f)). One can notice that the distributions are rather similar and, in particular, their widths $\Delta\mathrm{QS}$ of 1.65 mm s^{-1} are nearly equal, except in the higher QS region, where additional weak oscillations of $P(\mathrm{QS})$ appear in the 4.2 K case. From the overall similarity of these two distributions $P(\mathrm{QS})$ we infer that the effect on $P(\mathrm{QS})$ of cooling sample p4 (RTA) to 4.2 K is nearly the same as applying a field of 1.25 T to this sample at RT. This means that the hyperfine magnetic field, B_{hf}, that acts on the ^{57}Fe nuclei at 4.2 K in addition to the (nearly T-independent) electric quadrupole interaction, is of similar magnitude as the external field (1.25 T). Now, since we have evidence for the existence of a small hyperfine magnetic field in sample p4 (RTA) at 4.2 K, we conclude that magnetic ordering exists in sample p4 (RTA) at 4.2 K. The weakness of the hyperfine field (of the order of 1–1.5 T) can be due to a very small Fe atomic moment and/or a low magnetic ordering temperature in this sample. The superparamagnetic-type S-shaped magnetization curve observed at 20 K (figure 5(a2)) suggests that the intrinsic magnetic ordering temperature of sample p4 (RTA) is above 20–30 K. We like to emphasize again that no secondary phase formation (precipitates) could be detected by XRD on sample p4 in the as-implanted state and after RTA (figure 1). Therefore our combined structural and magnetic investigations provide strong evidence that sample p4 (RTA) is a real dilute magnetic semiconductor (DMS), though with a low magnetic

ordering temperature (above 20–30 K) and a small magnetic hyperfine field (∼1 T) at 4.2 K. Similarly the excess width in $P(\mathrm{QS})$ of $\delta\Delta\mathrm{QS} \approx 0.6$ mm s^{-1}, which is observed in figures 7(a) and (b) for sample p4 in the as-implanted state by cooling from RT ($\Delta\mathrm{QS} \approx 1.6$ mm s^{-1}) to 4.2 K ($\Delta\mathrm{QS} \approx 2.2$ mm s^{-1}), also may be interpreted as originating from a small hyperfine magnetic field (of the order of ∼1–1.5 T) due to magnetic ordering at 4.2 K in this DMS. Due to the complexity of the mixed hyperfine interactions at 4.2 K it is difficult to derive definite Mössbauer parameters (by simulation of CEM spectra), since no single-valued solutions for all the hyperfine parameters exist [53].

In conclusion we may claim that there is evidence for sample p4 being a real diluted magnetic semiconductor, for which Fe_3Si precipitation does not play a role as evidenced by XRD. High-resolution TEM measurements will be performed in the future to definitely exclude second-phase precipitations.

3.4.3. Detection of Fe_3Si. The RT CEM spectrum of the as-implanted high-dose sample p-hd is shown in figure 8(a), together with the 4.2 K CEM spectra of the annealed samples p5 and p3 (figures 8(b) and (c), respectively). All spectra show magnetic hyperfine splittings and a central doublet feature. The spectra were suitably fitted with one central paramagnetic doublet (Dbl) and nine sextets with Lorentzian lines (D0, D, A1–A7). According to the identification of the cubic Fe_3Si phase by our XRD measurements on these samples, the sextets were assigned to ^{57}Fe atoms residing in different sublattices of metallic Fe_3Si with a certain number of silicon and iron nearest neighbours. However, it has to be mentioned that sextet D0 (which has a small relative area of 0–6%) can simultaneously be assigned to metallic α-Fe. In x-ray diffraction the (110) α-Fe peak lies nearly at the same angular position as the (220) Fe_3Si reflection, and the TEM results also do not exclude metallic Fe. We like to emphasize that although the measurement statistics for sample p3 (figure 8(c)) are rather modest, we applied the fits for all samples in accordance with the hyperfine parameters of the various Fe_3Si sextets, and no inconsistency was observed.

Between a silicon content of 12.5 and 31 at.% the ordered $D0_3$ structure may be formed [54, 55] in Fe–Si alloys. In the perfectly chemically ordered case this phase exhibits only two iron sites. The corners of the cubic lattice are designated as site A. The body-centred sites are designated as site D. One half of the D sites is regularly occupied with Fe and the other half with Si atoms. An iron atom on the D-site has eight Fe nearest neighbours and six Si next-nearest neighbours. An iron atom on the A-site has four Fe and four Si as nearest neighbours and six Fe as next-nearest neighbours. Mössbauer spectra of the ideal $D0_3$ structure at RT exhibit two magnetically split sextets with a hyperfine field of $B_{\mathrm{hf}} = 20.0$ T for site A and $B_{\mathrm{hf}} = 30.9$ T for site D [56]. The local magnetic moments of the iron atoms on the A and D sites are 1.07 μ_{B} and 2.23 μ_{B}, respectively [57]. In the following discussion we use a certain notation for specifying the lattice sites: A_n ($n = 1, 2, \ldots, 7$) represents an iron atom in the A sublattice with n silicon atoms as nearest neighbours, D0 represents an iron atom in the D sublattice having zero Si nearest neighbours and zero Si next-nearest neighbours, iron designated as D has zero Si nearest neighbours, but 1–6 silicon atoms as next-nearest neighbours. This gives a total of nine magnetically split sextets. Our model is similar to that of Rixecker *et al* [55]. The CEM spectra in figure 8 were fitted with this model. The fitting of these spectra required the use of all sextets (D0, D, A1–A7), with the exception of D0 and A6 for sample p-hd at RT (figure 8(a)), and of A5 for both samples p5 and p3 at 4.2 K (figures 8(b), (c)). In addition to these sextets two broad Lorentzian lines for an asymmetric central paramagnetic quadrupole doublet (Dbl) had to be fitted to the spectra in figure 8. The Mössbauer spectral parameters obtained from figure 8 are given in table 3. It is problematic to achieve an unambiguous fit for the central part of the spectra, since the relative spectral

Table 3. Mössbauer spectral parameters of sample p-hd at RT and of samples p3 and p5 after RTA, measured at 4.2 K. The parameters were obtained from figure 8 by least-squares fitting of ten subspectra to the CEM spectrum of each sample. δ = isomer shift relative to α-Fe at RT, QS = quadrupole splitting of the doublet, B_{hf} = hyperfine magnetic field, Γ = full linewidth at half maximum, area = relative spectral area (relative intensity).

Subspectrum	δ (mm s^{-1})	QS (mm s^{-1})	B_{hf} (T)	Γ (mm s^{-1})	Area (%)
Sample p-hd, as implanted, T = RT					
Dbl	0.16(1)	0.89(7)	—	0.67(2)	33(4)
D0	0.01	—	33.0	0.65(1)	0.0
D	0.11	—	31.0	0.65(1)	6.3(5)
A1	0.13	—	28.17(6)	0.65(1)	16.9(4)
A2	0.16	—	23.92(5)	0.65(1)	17.2(2)
A3	0.19	—	18.8(1)	0.65(1)	9.6(7)
A4	0.22	—	15.7(6)	0.65(1)	2.7(7)
A5	0.25	—	11.0(1)	0.65(1)	9.1(4)
A6	0.28	—	6.6(9)	0.65(1)	0(1)
A7	0.31	—	2(1)	0.65(1)	5(3)
Sample p5, annealed, T = 4.2 K					
Dbl	0.25(3)	0.79(3)	—	0.89(3)	40(4)
D0	0.11	—	34.0	0.36	4.6(6)
D	0.21	—	32.0	0.36	5.3(6)
A1	0.24	—	28(1)	0.36	5.1(6)
A2	0.26	—	24.9(1)	0.36	6.8(5)
A3	0.31	—	21.03(6)	0.36	14.1(6)
A4	0.34	—	17.0(2)	0.36	4.3(6)
A5	0.36	—	13.0	0.36	0.0
A6	0.39	—	6.7(1)	0.36	12.5
A7	0.41	—	3.6(2)	0.36	7(3)
Sample p3, annealed, T = 4.2 K					
Dbl	0.25	0.86(2)	—	0.99(4)	62(3)
D0	0.11	—	34.0	0.36	6(1)
D	0.21	—	32.0	0.36	4(1)
A1	0.24	—	28.2(2)	0.36	4(1)
A2	0.26	—	24.8(2)	0.36	6(1)
A3	0.31	—	21.0(1)	0.36	11(1)
A4	0.34	—	18(1)	0.36	1(1)
A5	0.36	—	13.2	0.36	0.0
A6	0.39	—	6.8	0.36	4(2)
A7	0.41	—	3.6	0.36	1(2)

contribution of the doublet (Dbl) is not known in advance, and the sextets with small hyperfine fields (like A6 and A7) overlap with the doublet in this region. Since there is more ^{57}Fe in samples p3, p5 and p-hd (in this order), at least the trend of the decreasing relative spectral area (relative intensity) of the doublet seems reasonable because one may expect a higher amount of the Fe_3Si phase with increasing implantation dose (and, consequently, a smaller amount of relaxing superparamagnetic Fe_3Si or Fe particles, causing the doublet). Referring to [55] one may use a binomial distribution in order to calculate the probabilities for a specific iron environment, depending on the silicon content. The comparison with our data yielded no definite agreement of the measured relative spectral areas of the sextets with the calculated

probabilities of Fe environments for a specific silicon content. This is not surprising, since the Fe concentration is distributed inhomogeneously over the depth in our samples. However, since we had to use nearly all sextets D0, D, A1–A7 to obtain a good fitting one comes to the conclusion that the disordered B2 phase of Fe_3Si was created in our samples. It is a characteristic feature of the B2 phase that all of these sextets occur independent of the specific silicon content. If we had an ordered $D0_3$ phase, sextets A5–A8 would be missing for a silicon content of less than 25 at.%, and sextets A0–A3 would be missing for a silicon content of more than 25 at.%. This is certainly not the case here.

4. Conclusions

Mostly p-type 6H-SiC(0001) substrates were implanted with different doses of ^{57}Fe at 100 keV or 200 keV beam energy. Rapid thermal annealing (RTA) causes a shift of the ^{57}Fe concentration-depth profile towards the sample surface, which is explained via the kick-out mechanism (initially proposed for the diffusion of boron in Si and SiC). Mössbauer (CEM) spectra at RT and 4.2 K, taken on the as-implanted samples, exhibit asymmetric quadrupole-split doublets with isomer shifts typical for the metallic Fe state (Fe^0 state) or for the low-spin Fe^{II} valence state. The high-dose implanted sample p-hd (2×10^{17} cm^{-2}, 100 keV) showed a magnetic hyperfine splitting typical for the Fe_3Si phase, even at RT. For a dose $\geqslant 2 \times 10^{16}$ cm^{-2} and after RTA, XRD and TEM confirmed the formation of Fe_3Si nanoclusters with a large distribution of particle sizes up to ∼5 nm, which maintain an epitaxial relationship with the SiC matrix. Apart from Fe_3Si (and possibly a small fraction of metallic Fe) no additional phase segregations (e.g. of iron carbides or ternary compounds) were detected. Superparamagnetic blocking temperatures were estimated via FC–ZFC magnetization curves, and confirmed by hysteresis loops, with the highest T_B (∼400 K) and the most dispersed particle size distribution obtained for a dose of 2×10^{16} cm^{-2} at 100 keV. For higher doses T_B drops (e.g., 220 K for 3×10^{16} cm^{-2} at 200 keV) and the particle size distribution is more uniform. The high-dose implanted sample is not assumed to be superparamagnetic, but rather a ferromagnetic Fe_3Si phase. The low-temperature CEM spectra taken on annealed samples containing Fe_3Si nanoparticles prove that the atomically disordered B2 phase of Fe_3Si (and possibly a small fraction of metallic Fe) is responsible for superparamagnetism in this ion-implanted system. For the lowest dose (1×10^{16} cm^{-2} at 200 keV) the low-temperature CEM spectra (at 4.2 K) provide strong evidence for the presence of a small hyperfine magnetic field, presumably due to magnetic ordering. For this lowest dose T_B was found to be lower than ∼20 K; however, no precipitates were detectable by XRD. We suggest that for a possible DMS system, consisting of Fe-implanted SiC, the maximum Fe concentration has to be kept in the range of 1–3 at.% in order to prevent second phase segregations. A different annealing procedure (lower temperatures) might be a second possibility for producing a DMS.

Acknowledgments

The expertise and technical assistance of U von Hörsten (Duisburg) is gratefully acknowledged. Work supported by Deutsche Forschungsgemeinschaft (DFG) under Ke 273/19-1 and Re 868/7-1.

References

[1] Ohno H 1998 *Science* **281** 951
[2] Datta S and Das B 1990 *Appl. Phys. Lett.* **56** 665

[3] Ohno Y, Young D K, Beschoten B, Matuskara F, Ohno H and Awschalom D D 1999 *Nature* **402** 790
[4] Buyanova I A, Izadifard M, Chen W M, Kim J, Ren F, Thaler G, Abernathy C R, Pearton S J, Pan C C, Chen G T, Chyi J I and Zavada J M 2004 *Appl. Phys. Lett.* **84** 2599
[5] Buyanova I A, Ivanov B, Monemar B, Chen W M, Toropov A A, Terent'ev Ya V, Sorokin S V, Lebedev A V, Ivanov S V and Kop'ev P S 2002 *Appl. Phys. Lett.* **81** 2196
[6] Oestreich M, Hübner J, Hägele D, Klar P J, Heimbrodt W, Rühle W W, Ashenford D E and Lunn B 1999 *Appl. Phys. Lett.* **74** 1251
[7] Fiederling R, Keim M, Reuscher G, Ossau W, Schmidt G, Waag A and Molenkamp L W 1999 *Nature* **402** 787
[8] Jonker B T, Park Y D, Bennett B R, Cheong H D, Kioseoglou G and Petrou A 2000 *Phys. Rev.* B **62** 8180
[9] Kayanuma K, Debnath M C, Souma I, Chen Z, Murayama A, Kobayashi M, Miyazaki H and Oka Y 2002 *Phys. Status Solidi* b **229** 761
[10] Schmidt G, Ferrand D, Molenkamp M, Filip A T and van Wees B J 2000 *Phys. Rev.* B **62** R4790
[11] Hanbicki A T, Jonker B T, Itskos G, Kioseoglou G and Petrou A 2002 *Appl. Phys. Lett.* **80** 1240
[12] Motsnyi V F, De Boeck J, Das J, Van Roy W, Borghs G, Goovaerts E and Safarov V I 2002 *Appl. Phys. Lett.* **81** 265
[13] Hanbicki A T, van't Erve O M, Magno R, Kioseoglou G, Li C H, Itskos G, Mallory R, Yasar M and Petrou A 2003 *Appl. Phys. Lett.* **82** 4092
[14] Van Dorpe P, Motsnyi V F, Nijboer M, Goovaerts E, Safarov I, Das J, Van Roy W, Borghs G and De Boeck J 2003 *Japan. J. Appl. Phys.* **42** L502
[15] Toyosaki H, Fukumura T, Ueno K, Nakano M and Kawasaki M 2005 *Japan. J. Appl. Phys.* **44** L896
[16] Van Roy W, Van Dorpe P, Motsnyi V, Liu Z, Borghs G and De Boeck J 2004 *Phys. Status Solidi* b **241** 1470
[17] Gerhardt N C, Hövel S, Brenner C, Hofmann M R, Lo F-Y, Reuther H, Wieck A D, Schuster E, Keune W and Westerholt K 2005 *Appl. Phys. Lett.* **87** 032502
[18] Jiang X, Wang R, Shelby R M, Macfarlane R M, Banks S R, Harris J S and Parkin S S P 2005 *Phys. Rev. Lett.* **94** 056601
[19] Zhu H J, Ramsteiner M, Kostial H, Wassermeier M, Schönherr H P and Ploog K H 2001 *Phys. Rev. Lett.* **87** 016601
[20] Ionescu A, Vaz C A F, Trypiniotis T, Gürtler C M, Garcia-Miquel H, Bland J A C, Vickers M E, Dalgliesh R M, Lanridge S, Bugoslavsky Y, Miyoshi Y, Cohen L F and Ziebeck K R A 2005 *Phys. Rev.* B **71** 094401
[21] Munekata H, Ohno H, von Molnar S, Segmüller A, Chang L L and Esaki L 1989 *Phys. Rev. Lett.* **63** 1849
[22] Ohno H, Shen A, Matsukura F, Oiwa A, Endo A, Katsumoto S and Iye Y 1996 *Appl. Phys. Lett.* **69** 363
[23] Foxon C T, Campion R P, Edmonds K W, Zhao L, Wang K, Farley N R S, Staddon C R and Gallagher B L 2004 *J. Mater. Sci.* **15** 727
[24] Dietl T, Ohno H and Matsukura F 2001 *Phys. Rev.* B **63** 195205
[25] Ueda K, Tabata H and Kawai T 2001 *Appl. Phys. Lett.* **79** 988
[26] Sonoda S, Shimizu S, Sasaki T, Yamamoto Y and Hori H 2002 *J. Cryst. Growth* **237** 1358
[27] Hebard A F, Rairigh R P, Kelly J G, Pearton S J, Abernathy C R, Chu S N G and Wilson R G 2004 *J. Phys. D: Appl. Phys.* **37** 511
[28] Potzger K, Zhou S, Reuther H, Mücklich A, Eichhorn F, Schell N, Skorupa W, Helm M, Fassbender J, Herrmannsdörfer T and Papageorgiou T P 2006 *Appl. Phys. Lett.* **88** 052508
[29] Sasaki T, Sonoda S, Yamamoto Y, Suga K, Shimizu S, Kindo K and Hori H 2002 *J. Appl. Phys.* **91** 7911
[30] Kuwabara S, Kondo T, Chikyow T, Ahmet P and Munekata H 2001 *Japan. J. Appl. Phys.* **40** L724
[31] Ploog K H, Dhar S and Trampert A 2003 *J. Vac. Sci. Technol.* B **21** 1756
[32] Shaposhnikov V I and Sobolev N A 2004 *J. Phys.: Condens. Matter* **16** 1761
[33] Miao M S and Lambrecht R L 2003 *Phys. Rev.* B **68** 125204
[34] Zhangi D, Traverse A, Gautrot S and Kaitasov O 2001 *J. Mater. Res.* **16** 512
[35] Theodoropoulou N, Hebard A F, Chu S N G, Overberg M E, Abernathy C R, Pearton S J, Wilson R G, Zavada J M and Park Y D 2002 *J. Vac. Sci. Technol.* A **20** 579
[36] Theodoropoulou N, Hebard A F, Chu S N G, Overberg M E, Abernathy C R, Pearton S J, Wilson R G, Zavada J M and Park Y D 2002 *J. Appl. Phys.* **91** 7499
[37] Shinjo T and Keune W 1999 *J. Magn. Magn. Mater.* **200** 598
[38] See, for instance Dickson D P E and Berry F 1986 *Mössbauer Spectroscopy* (Cambridge: Cambridge University Press)
[39] Brand R A 1987 *Nucl. Instrum. Methods Phys. Res.* B **28** 398 (the NORMOS program is available from WISSEL GmbH, D-82319 Starnberg, Germany)
[40] Yoshitake T, Nakagauchi D, Ogawa T, Itakura M, Kuwano N, Tomokiyo Y, Kajiwara T and Nagayama K 2005 *Appl. Phys. Lett.* **86** 262505
[41] Fanciulli M, Weyer G, von Känel H and Onda N 1994 *Phys. Scr.* T **54** 16

[42] Lipson H and Petch N J 1940 *J. Iron Steel Inst.* **142** 95
[43] Zetterling C K (ed) 1998 *Process Technology for Silicon Carbide Devices* (London: INSPEC)
[44] Bracht H, Stolwijk N A, Laube M and Pensl G 2000 *Appl. Phys. Lett.* **77** 3188
[45] Miao M S and Lambrecht R L 2003 *Phys. Rev.* B **68** 125204
[46] Pajic D, Zadro K, Vanderberghe R E and Nedkov I 2004 *J. Magn. Magn. Mater.* **281** 353
[47] Park Y D, Hanbicki A T, Irwin S C, Hellberg C S, Sullivan J M, Mattson J E, Ambrose T F, Wilson A, Spanos G and Jonker B T 2002 *Science* **295** 651
[48] Das Sarma S, Hwang E H and Kaminski A 2003 *Phys. Rev.* B **67** 155201
[49] See, for instance Vineze I, Kaptas D, Kemeng T, Kiss L F and Balogh J 1994 *Phys. Rev. Lett.* **73** 496
[50] Greenwood N N and Gibb T C 1971 *Mössbauer Spectroscopy* (London: Chapman and Hall)
[51] McHargue C J, Perez A and McCallum J C 1991 *Nucl. Instrum. Methods* B **59** 1362
[52] Horton L L, Bentley J, Romana L, McHargue C J and McCallum J C 1992 *Nucl. Instrum. Methods* B **65** 345
[53] Barb D and Meisel W 1980 *Grundlagen und Anwendungen der Mössbauerspektroskopie* (Berlin: Akademie-Verlag) p 136 (in German)
[54] Stearns M B 1963 *Phys. Rev.* **129** 1136
[55] Rixecker G, Schaaf P and Gonser U 1993 *Phys. Status Solidi* a **139** 309
[56] Miyazaki M, Ichikawa M, Komatsu T and Matusita K 1992 *J. Appl. Phys.* **71** 2368
[57] Moss J and Brown P J 1972 *J. Phys. F: Met. Phys.* **2** 358